Journal of
Synchrotron
Radiation

ISSN 0909-0495

Received 24 February 2005
Accepted 14 July 2005

Performance of a dispersion-compensating scanning X-ray spectrometer for Compton profile measurements

N. Hiraoka,[a]*‡ T. Buslaps,[a] V. Honkimäki[a] and P. Suortti[b]

[a]Synchrotron Radiation Facility (ESRF), BP 220, 38043 Grenoble CEDEX 9, France, and [b]Department of Physics, University of Helsinki, PO Box 64, FIN-0014 Helsinki, Finland. E-mail: hiraoka@spring8.or.jp

A new X-ray spectrometer has been constructed for Compton profile measurements at beamline ID15B of the ESRF. The spectrometer is based on a novel idea, dispersion compensation, which was proposed earlier. A cylindrically bent Laue monochromator focuses ~90 keV synchrotron radiation at about 0.7 m before the sample, and produces a well defined energy or wavelength gradient on the sample. A cylindrically bent Laue analyser almost perfectly compensates this wavelength gradient. Using an Al sample, it has been confirmed that the new spectrometer improves the counting rate by a factor of two compared with the previously constructed 30 keV and 60 keV spectrometers, with a comparable momentum resolution. Because of reduced absorption owing to use of high-energy X-rays, the enhancement of the counting rate is spectacular for heavy-element materials.

Keywords: X-ray spectrometer; Compton scattering; dispersion compensation.

1. Introduction

Compton-scattered X-rays from a material provide us with information about the electron momentum distribution. Within the impulse approximation (Eisenberger & Platzman, 1970), the energy of scattered X-rays (ε_2) is simply determined by the energy of the incident X-rays (ε_1), the scattering angle (Θ) and the primary electron momentum ($\mathbf{p}_1$),

$$\varepsilon_2 = \frac{\varepsilon_1 + \mathbf{p}_1 \cdot \mathbf{K}\, m^{-1}}{1 + \varepsilon_1(1 - \cos\Theta)\, m^{-1}c^{-2}}, \qquad (1)$$

where m and c are the electron mass and the velocity of light, respectively. The $\mathbf{p}_1 \cdot \mathbf{K}$ term gives the projection of $\mathbf{p}_1$ onto the scattering vector, $\mathbf{K}$, which is defined by ε_1, ε_2 and Θ. Therefore, the energy spectrum provides the momentum density $[\rho(\mathbf{p}_1)]$ projected onto $\mathbf{K}$, *i.e.* the Compton profile,

$$J(p_{1z}) = \iint \rho(\mathbf{p}_1)\, \mathrm{d}p_{1x}\, \mathrm{d}p_{1y}. \qquad (2)$$

The z-axis is typically taken parallel to $\mathbf{K}$, and p_{1z} is the z-component of $\mathbf{p}_1$, *i.e.* the projection of $\mathbf{p}_1$ onto $\mathbf{K}$ ($p_{1z} = \mathbf{p}_1 \cdot \mathbf{K}/|\mathbf{K}|$). When $\mathbf{p}_{1(z)} \rightarrow 0$, and the wavelengths of the incident X-rays (λ_1) and scattered X-rays (λ_2) are used, (1) yields a simple result for the Compton peak,

$$\lambda_2 = \lambda_1 + h(1 - \cos\Theta)\, m^{-1}c^{-1}, \qquad (3)$$

where h is the Planck constant. This relation is important for the operation of the dispersion-compensating spectrometer, as discussed later. In order to investigate momentum densities in materials, various kinds of X-ray spectrometers have been developed for Compton scattering experiments. Currently two methods are used for energy analysis of scattered radiation. One uses a Ge solid-state detector (SSD) and the other uses a crystal analyser. The latter makes possible experiments with three to five times higher resolution. This improvement is very significant for examining solids, particularly in investigating Fermi surfaces in momentum space. However, the efficiency of a crystal analyser is rather low. Therefore, there was limited application of this kind of spectrometer to heavy-element materials, which strongly absorb the X-rays, before the recent advent of intense high-energy synchrotron radiation sources.

Compton spectrometers using a crystal analyser can be classified into either the Cauchois type or the scanning type. In the Cauchois type, all the components are basically stationary. A spectrum is recorded as a function of position on a position-sensitive detector (Loupias & Petiau, 1980; Shiotani *et al.*, 1989; Berthold *et al.*, 1992; Sakurai *et al.*, 1992; Hiraoka *et al.*, 2001; Itou & Sakurai, 2004). In the scanning type, a spectrum is recorded as a function of the Bragg angle of the crystal analyser (θ_A), where the analyser and the detector move along several axes, synchronized with θ_A (Suortti *et al.*, 1999). If each component performs adequately, one can have similar resolutions and count rates using both types of spectrometers. However, problems arise in the high-energy region. High-

‡ Present address: Taiwan Beamline, SPring-8, 1-1-1 Kouto, Mikazuki, Sayo, Hyogo 679-5198, Japan.

energy X-rays of $\sim$100 keV are not focused or reflected well by bent crystals, and are detected with less efficiency and poor spatial resolution by position-sensitive detectors compared with X-rays of $\leq$30 keV.

As for the monochromator, the Rowland circle geometry with a bent Bragg crystal has been used widely so far for both types of spectrometers. Here, a light source and a sample are placed on the Rowland circle defined by the bending radius of the monochromator. The finite thickness of the crystal, however, generally causes a rather large aberration, *i.e.* a large focal size for high-energy X-rays. For scanning spectrometers, the focusing properties are particularly important because the resolution is mainly determined by the focal size or the width of the slits placed at the focal point. Schulze *et al.* (1998) demonstrated the ability of a cylindrically bent Laue crystal to eliminate this aberration. Nevertheless, it was not straightforward to apply a bent Laue monochromator to spectrometers for Compton scattering. This is because the light source can no longer be placed on the Rowland circle in the Laue geometry, and thus the reflected beam has a rather wide range of energies, or a large wavelength gradient.

A few years ago we proposed a new combination of a monochromator, an analyser and a detector, so as to compensate the wavelength gradient and to optimize a scanning spectrometer in the $\sim$100 keV region (Suortti *et al.*, 2001). In the report, we showed the potential of the dispersion-compensating spectrometer with results of a test experiment. After having implemented several improvements, the spectrometer is now used for actual experiments. In the present report we show the current performance of the dispersion-compensating spectrometer. Some improvements are still necessary, but the spectrometer is already close to its ultimate performance.

2. Dispersion-compensating spectrometer

The idea of the dispersion-compensating spectrometer has already been described in our earlier work (Suortti *et al.*, 2001). We repeat some essential parts here to help understand the principle. Fig. 1 illustrates the spectrometer. The monochromator is a cylindrically bent Laue crystal. The bent Laue monochromator leads to high reflectivity, an optimized bandpass and aberration-free focusing. As already mentioned, the Laue monochromator also has a wide range of θ_B ($\theta_{M1} \rightarrow \theta_{M2}$ in Fig. 1), *i.e.* a large energy or wavelength gradient along the horizontal axis ($d\lambda/ds$), where λ is the wavelength and s is a position along the tangential axis to the curvature of the crystal (see Fig. 1). The wavelength gradient on the monochromator is given by

$$\begin{aligned} d\lambda/ds &= 2d_M \cos\theta_M \, (d\theta_M/ds) \\ &= 2d_M \cos\theta_M \, (P_0 - P) \, P^{-1} P_0^{-1}, \end{aligned} \tag{4}$$

where d_M is the d-spacing of the monochromator (Si 511), P is the distance between the source and the monochromator, and $P_0 = R_M \cos(\theta_M + \chi_M)$. R_M is the bending radius and χ_M is the asymmetric cut of the monochromator. Equation (4) is equivalent to equation (4) of Suortti *et al.* (2001). The beam converges to the focus at a distance Q from the monochromator, and at the sample the gradient is reversed and magnified by a factor Q/L, where L is the distance between the focal point and the sample. The wavelength gradient on the sample, $(d\lambda/dx)_M$, is

$$(d\lambda/dx)_M = (d\lambda/ds)(Q/L), \tag{5}$$

where x is a position along the horizontal axis on the sample. Similarly, the scattered beam reflected by the analyser has a wavelength gradient $(d\lambda/dx)_A$ owing to the width of the beam at the sample. The width of the analyser reflectivity curve can be adjusted by the asymmetric cut χ_A (Suortti *et al.*, 1997). For the energy resolution required in the present case, χ_A is small, only about 1.5°. The Bragg angle, θ_A, is also small at high photon energies, so that the dispersion relation simplifies to

$$\begin{aligned} (d\lambda/dx)_A &= 2d_A \cos\theta_A \, (d\theta_A/dx) \\ &= 2(d_A/R_A) \cos\theta_A, \end{aligned} \tag{6}$$

where d_A and θ_A are the d-spacing of the analyser (Si 400) and the Bragg angle, respectively, and R_A is the bending radius. This equation is equivalent to equation (5) of Suortti *et al.* (2001) at the limit of small θ_A and χ_A. When the dispersion-compensation condition is fulfilled, the two gradients coincide, *i.e.* $(d\lambda/dx)_M = (d\lambda/dx)_A$. If perfect gradients and their

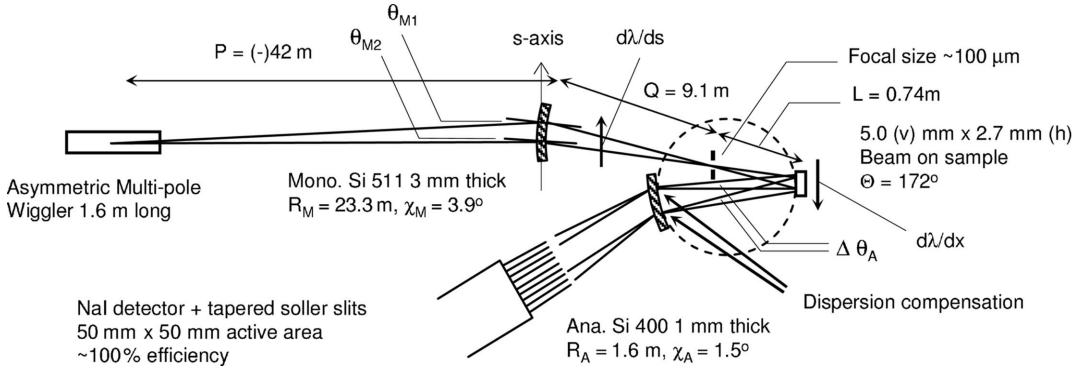

Figure 1
Geometry and parameters of the dispersion-compensating spectrometer, describing the light source, the monochromator, the analyser and the detector.

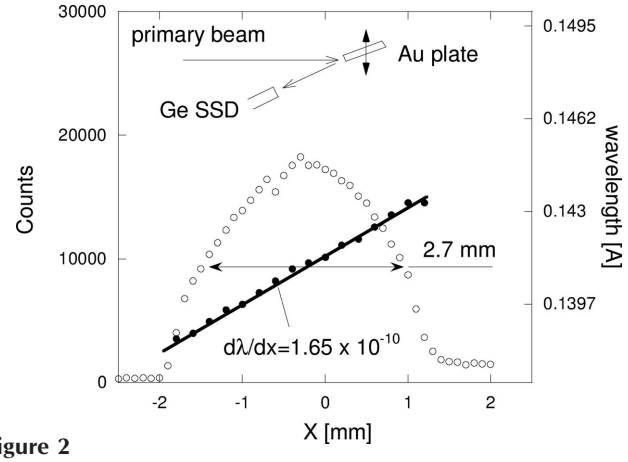

Figure 2
Wavelength gradient (black circles) and corresponding intensities (white circles) on the sample.

compensation are achieved, the spectrum measured as a function of θ_A shows a single peak, like the experimental result obtained for elastic scattering (see Fig. 3), but the analyser actually reflects X-rays of different energies.

The condition of the dispersion compensation is precisely valid only for one gradient. Once the dispersion compensation is optimized for the elastic scattering of X-rays, it is seen from (3) that the gradient is the same at $p_{1z} = 0$, so that the dispersion compensation is exact. Away from the Compton peak, there is an extra broadening of the resolution function owing to the uncompensated dispersion, but the effect is very small, only a few percent of the resolution function, which can be neglected (Suortti *et al.*, 2001). It is noted that (5) assumes the *x*-axis on the sample to be parallel to the *s*-axis on the monochromator. If the *x*-axis or the sample surface is rotated, the dispersion-compensation condition should be re-adjusted by changing R_A.

3. Performance tests

3.1. Wavelength gradient

The wavelength gradient and the intensity distribution of the incident beam were measured by the following experiment. A 200 µm-thick gold plate, placed at the sample position, was rotated so that the surface normal was at an angle of 60° from the incident beam, and the edge of the plate was irradiated by X-rays (see the inset in Fig. 2). Using a Ge SSD, placed at a scattering angle of 150°, the elastic scattering spectrum was collected as a function of the position of the gold plate. In this geometry, scattering from the surfaces was strongly absorbed, and the signal was dominated by the scattering from the edge. Hence, it was possible to obtain the wavelength gradient and the intensity distribution with a spatial resolution of 200 µm. Fig. 2 plots the peaks and integrated intensities of spectra as a function of the position *x*. Least-squares fitting shows that $(d\lambda/dx)_M = 1.65$ Å m^{-1} = 1.65×10^{-10}. This agrees well with the gradient of 1.70 Å m^{-1} expected from the geometry of the monochromator. Using the observed $(d\lambda/dx)_M$ we obtain $R_A = 1.60$ m from (6).

Table 1
Comparison of the theoretical and experimental resolutions.

$\Delta\varepsilon_{geo}$ is the energy width arising from the slit width, and $\Delta\varepsilon_{M(A)}$ is the band width of the monochromator (analyser). $\Delta\varepsilon_{tot}$ was calculated by $(\Delta\varepsilon_{geo}^2 + \Delta\varepsilon_M^2 + \Delta\varepsilon_A^2)^{1/2}$. The momentum resolutions are those at the Compton peak. a.u. means atomic units: 1 a.u. = 1.99×10^{-24} kg m s^{-1}.

Slit width (µm)	$\Delta\varepsilon_{geo}$ (eV)	$\Delta\varepsilon_M$ (eV)	$\Delta\varepsilon_A$ (eV)	$\Delta\varepsilon_{tot}$ (eV)	$\Delta\varepsilon_{exp}$ (eV)	$\Delta P_{1z\,exp}$ (a.u.)
100	100	25	60	119	117	0.08
60	60	25	60	88	91	0.06

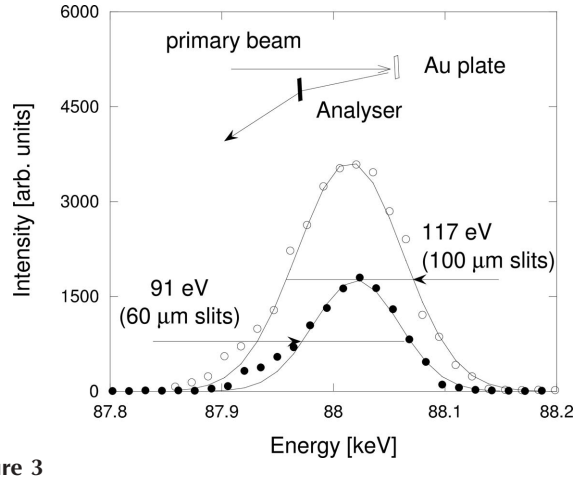

Figure 3
Elastic lines from Au with a 100 µm-wide collimating slit (white circles) and with a 60 µm-wide slit (black circles).

3.2. Resolution function

As already mentioned, the line shape of the elastic line provides the exact resolution function of a Compton profile at $p_{1z} = 0$. Fig. 3 shows the elastic lines from the gold plate, which was mounted so that the surface normal was parallel to the scattering vector (see the inset). For a scanning spectrometer, the resolution is a function of the sample thickness (t) or the penetration length of X-rays (l_p) in the sample. In the geometry of our spectrometer, the deterioration of the resolution is seen when both t and l_p are ≥ 1 mm. The gold plate, having a much smaller l_p, $\sim$40 µm, simulates an ideal sample. Using a 100 µm-wide slit, we have obtained a resolution of 120 eV (FWHM). This corresponds to a momentum resolution of 0.08 a.u. at the Compton peak (here a.u. means atomic units and 1 a.u. = 1.99×10^{-24} kg m s^{-1}). Similarly, we have obtained a resolution of 90 eV (0.06 a.u.) with a 60 µm-wide slit. The 60 µm-wide slit simply causes an intensity loss of 40% compared with the 100 µm-wide slit. Table 1 shows several main contributions to the resolutions. The observed resolutions agree well with our expectations.

3.3. Compton profiles

Fig. 4(*a*) shows the Compton profile of Al. It was measured using a 100 µm-wide slit on a 0.5 mm-thick Al sample, using the 90 keV spectrometer. The scattering angle was 172°. The resolution of 0.08 a.u. is confirmed from the FWHM of the elastic line. The observed spectrum is almost perfectly repro-

duced with the valence-electron Compton profile based on band theory (Papanicolaou *et al.*, 1991), the core-electron Compton profile from the Hartree–Fock calculation (Biggs *et al.*, 1975), a multiple scattering spectrum obtained by Monte Carlo simulation (Fajardo *et al.*, 1998), and a parabolic background. The counting rate at the Compton peak was 1200 counts s^{-1} at ~60 mA storage-ring current.

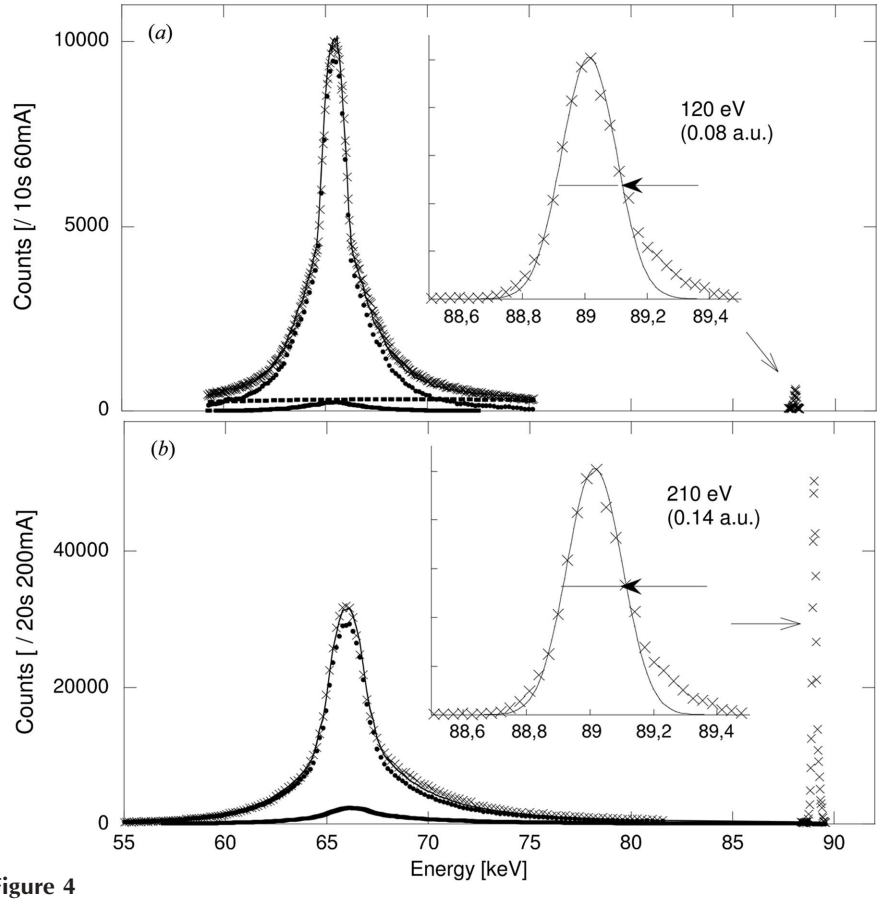

Figure 4
Measured Compton profiles (crosses) of (*a*) Al and (*b*) Sr_2RuO_4, compared with theory (thin solid lines). The theoretical spectra are obtained by summing the theoretical Compton profiles (dots), the multiple scattering contributions (thick solid lines) and the background (thick broken line). The theoretical Compton profile of Al is the sum of the valence-electron (Papanicolaou *et al.*, 1991) and the core-electron (Biggs *et al.*, 1975) contributions. The theoretical Compton profile of Sr_2RuO_4 was calculated based on band theory (Hiraoka, Buslaps, Honkimäki, Itou *et al.*, 2005). The background is not shown for (*b*) because it was negligible. The insets show the elastic lines (crosses). The solid lines are the fitting results with Gaussian curves. The shoulders in the high-energy side arise from the imperfect dispersion compensation, mainly due to the penetration depth of X-rays in the samples.

One of most important comparisons is between the performance of the present 90 keV spectrometer and that of the previously constructed 60 keV and 30 keV ones having a standard Rowland circle geometry. The 60 keV spectrometer consists of a Si 311 monochromator and a Ge 440 analyser, while that of 30 keV consists of a Si 111 monochromator and a Si 400 analyser (see Suortti *et al.*, 1999). The slit widths of the 60 keV and 30 keV spectrometers are typically 200 μm, while that of the 90 keV spectrometers is 100 μm. The scattering angles are common, 172°, for the three spectrometers. The comparisons are summarized in Table 2. The counting rate is about twice the rate achieved with 60 keV and 30 keV conventional spectrometers. The resolution is better by a factor of ~2 than that of the 60 keV spectrometer, and the same as that of the 30 keV spectrometer. The background is 3% of the peak intensity, and most of the background is from air scattering around the sample. If we had used a vacuum chamber, already available at the beamline, the background would have been significantly reduced.

Compton profile measurements on heavy-element materials, utilizing high-energy synchrotron radiation are one of the biggest motivations for the construction of this spectrometer.

Table 2
Summary of the counting rates and resolutions.

Beam size in the 90 keV spectrometer is determined by the slits, placed 5 m behind the monochromator, according to the sample size, while those for the 30 and 60 keV spectrometers are determined by the slit just before the sample. ε_1 is the incident photon energy, t is the actual thickness of each sample, and l_p is the penetration depth of the X-rays: the smaller one gives the effective thickness, affecting the energy resolution. Averaged counting rates were taken between −3 and 3 atomic units (a.u.), *i.e.* 63.2 to 68.3 keV for ε_1 = 88.0 keV, 44.4 to 48.0 keV for ε_1 = 56.3 keV, and 25.3 to 27.5 keV for ε_1 = 29.4 keV. RC stands for the electron beam current in the storage ring.

Samples	ε_1 (keV)	Beam size (h × v) (mm)	t (mm)	l_p (mm)	Resolution (a.u.)	Count rate at peak (averaged) (s^{-1})
Al	88.3	5.0 × 2.7	0.5	8.4	0.08	1200 (560) at 60 mA RC
Al	56.3	5.0 × 0.2	0.5	5.4	0.15	600 (280) at 60 mA RC
Al	29.4	5.0 × 0.2	0.5	1.4	0.08	600 (280) at 60 mA RC
Mo_4O_{11}†	88.3	3.0 × 0.8	0.5	0.48	0.16	1500 (820) at 180 mA RC
$Ba_{0.6}K_{0.4}BiO_3$‡	88.3	5.0 × 1.5	2.0	0.19	0.12	1000 (520) at 180-mA RC
Sr_2RuO_4§	88.3	2.0 × 2.0	2.0	0.47	0.14	1000 (530) at 180 mA RC

† Hiraoka, Buslaps, Honkimäki, Guyot & Schlenker (2005). ‡ Hiraoka, Buslaps, Honkimäki, Minami & Uwe (2005). § Hiraoka, Buslaps, Honkimäki, Itou *et al.* (2005).

Fig. 4(*b*) shows the experimental Compton profile of an unconventional superconductor, Sr_2RuO_4, along with the theoretical Compton profile calculated based on band theory (Hiraoka, Buslaps, Honkimäki, Itou *et al.*, 2005). Reduced absorption in the ε_1 = 90 keV experiment increases the Compton scattering intensity by more than three and 15 times, compared with in the ε_1 = 60 keV and 30 keV experiments on this sample, respectively. Namely, the total improvement in the count rate is a factor of $\geq$6 and 30. In this experiment, almost perfect collimation was achieved for scattered X-rays from the sample mounted on the 20 K cryostat, and the background-to-signal ratio was $\sim$0.01%. The overall shape is almost perfectly reproduced without assuming any background. The resolution is deteriorated by a factor of about two compared with the experiment on Al. The extra peak broadening was due to a mismatch of the energy gradients of the monochromator and analyzer because of the following two reasons: firstly, the surface was not flat and, secondly, the Compton profile was measured for the [100] direction, which made an angle of 22° with the surface normal. This could be re-adjusted as mentioned at the end of the last section.

4. Summary and future improvements

The new Compton spectrometer, based on a novel idea, *i.e.* dispersion compensation, was constructed at beamline ID15 of the ESRF. This spectrometer has been confirmed with an Al sample to improve the counting rate by a factor of two with a resolution comparable with the conventional 60 keV and 30 keV spectrometers. The enhancement of the counting rate is spectacular in measurements for heavy-element materials owing to the reduced absorption of high-energy X-rays. The peak counting rate is $\sim$1000 counts s^{-1} for samples including 4*d* or 5*p* elements. With this counting rate, typically it is possible to reach a Compton profile with 100000 counts at the peak within a bin of 0.02 a.u. in half a day, and thus eight to ten Compton profiles in a beam time of one week. In fact, for all the samples shown in Table 2 (except for Al), the momentum densities were reconstructed from Compton profiles acquired in one week. They all showed significant results (Hiraoka, Buslaps, Honkimäki, Guyot & Schlenker, 2005; Hiraoka, Buslaps, Honkimäki, Minami & Uwe, 2005; Hiraoka, Buslaps, Honkimäki, Itou *et al.*, 2005).

Although the new spectrometer already shows high performance, there is still room for improvements. The first point is the cooling system of the monochromator. Most of the performance tests were made in the 16 bunch mode, where the average ring current was $\sim$60 mA. We also tried some tests in the normal mode, where the average ring current was 190–180 mA, but the counting rate did not increase linearly with the ring current, and the gain was 2.5 at most. Furthermore, the intensity distribution of the beam on a sample separates into several peaks, unlike the broad single peak in Fig. 2. An effective improvement for the cooling system does not only lead to an improved counting rate but may also provide a smaller focal size (theoretically, 30 µm is possible). This would make higher resolution possible without loss of beam intensity.

The second point is the scattering geometry. At present, the spectrometer has the so-called horizontal scattering geometry, where the analyser is placed at a scattering angle of 172° in the horizontal plane. In the vertical scattering geometry, where the analyser is below the incident beam, the resolution is independent of the penetration depth in the sample and of the orientation and/or the roughness of the irradiated surface. Therefore, the deterioration of the resolution, seen in the data of Sr_2RuO_4, should be eliminated. The project to modify the scattering geometry has already started.

We would like to thank T. Martin (ESRF) for helping us with monitoring the deformation of the analyser crystal with a two-dimensional scintillator. The data of Sr_2RuO_4 were taken in collaboration with Y. Sakurai (SPring-8) and Y. Maeno (Kyoto University).

References

Berthold, A., Mourikis, S., Schmitz, J. R., Schülke, W. & Schulte-Schrepping, H. (1992). *Nucl. Instrum. Methods*, A**317**, 373–382.
Biggs, F., Mendelsohn, L. B. & Mann, J. B. (1975). *Atom. Data Nucl. Data Tables*, **16**, 201–309.
Eisenberger, P. & Platzman, P. M. (1970). *Phy. Rev. A*, **2**, 415–423.
Fajardo, P., Honkimäki, V., Buslaps, T. & Suortti, P. (1998). *Nucl. Instrum. Methods*, B**134**, 337–345.
Hiraoka, N., Buslaps, T., Honkimäki, V., Guyot, H. & Schlenker, C. (2005). *Phys. Rev. B*, **71**, 125417-1–125417-5.
Hiraoka, N., Buslaps, T., Honkimäki, V., Itou, M., Sakurai, Y., Mao, Z. Q. & Maeno, Y. (2005). In preparation.
Hiraoka, N., Buslaps, T., Honkimäki, V., Minami, H. & Uwe, H. (2005). *Phys. Rev. B*, **71**, 205106-1–205106-6.
Hiraoka, N., Itou, M., Ohata, T., Mizumaki, M., Sakurai, Y. & Sakai, N. (2001). *J. Synchrotron Rad.* **8**, 26–32.
Itou, M. & Sakurai, Y. (2004). *AIP Conf. Proc.* **705**, 901–904.
Loupias, G. & Petiau, J. (1980). *J. Phys.* **41**, 265–271.
Papanicolaou, N. I., Bacalis, N. C. & Papaconstantopoulos, D. A. (1991). *Handbook of Calculated Electron Momentum Distributions, Compton Profiles, and X-ray Form Factors of Elemental Solids*, pp. 104–105. Boca Raton, FL: CRC Press.
Sakurai, Y., Ito, M., Urai, T., Tanaka, Y., Sakai, N., Iwazumi, T., Kawata, H., Ando, M. & Shiotani, N. (1992). *Rev. Sci. Instrum.* **63**, 1190–1193.
Schulze, C., Lienert, U., Hanfland, M., Lorenzen, M. & Zontone, F. (1998). *J. Synchrotron Rad.* **5**, 77–81.
Shiotani, N., Sakai, N., Itoh, F., Sakurai, M., Kawata, H., Amemiya, Y. & Ando, M. (1989). *Nucl. Instrum. Methods*, A**275**, 447–452.
Suortti, P., Buslaps, T., DiMichiel, M., Honkimäki, V., Lienert, U., McCarthy, J. E., Merino, J. M. & Shukla, A. (2001). *Nucl. Instrum. Methods*, A**467/468**, 1541–1544.
Suortti, P., Buslaps, T., Fajardo, P., Honkimäki, V., Kretzschmer, M., Lienert, U., McCarthy, J. E., Renier, M., Shukla, A., Tschentscher, Th. & Meinander, T. (1999). *J. Synchrotron Rad.* **6**, 69–80.
Suortti, P., Lienert, U. & Schulze, C. (1997). *AIP Conf. Proc.* **389**, 175–192.